Chemical Engineering Journal 496 (2024) 154103

Contents lists available at ScienceDirect

Chemical Engineering Journal

journal homepage: www.elsevier.com/locate/cej

Joule heating for structure reconstruction of hard carbon with superior sodium ion storage performance

Ziqing Song [a], Qiyan Du [a], Jing Chen [a], Jin Huang [a], Yue Chen [a], Lituo Zheng [a], Zhigao Huang [a,c], Hong Dai [b], Zhensheng Hong [a,c,*]

[a] Fujian Provincial Key Laboratory of Quantum Manipulation and New Energy Materials, College of Physics and Energy, Fujian Normal University, Fuzhou, Fujian, 350117, China
[b] College of Chemistry and Materials Science, Fujian Normal University, Fuzhou, Fujian, 350117, China
[c] Academy of Carbon Neutrality of Fujian Normal University, Fuzhou, 350117, China

ARTICLE INFO

Keywords:
Sodium ion batteries
Anode
Hard carbon
Joule heating
Structure reconstruction

ABSTRACT

Hard carbon anode for sodium ion batteries still remains many challenges including insufficient cycling life and initial Coulombic efficiency (ICE), weak rate capability and poor compatibility in common ester electrolytes. Here, we propose a Joule heating post-treatment including multifield sintering method to reconstruct the structure of hard carbon from thick graphene layers to more disordered vortex layer structure composed of thin and curved graphite-like domains. The molecular dynamics simulation and differential charge density distribution demonstrate the crucial effect of electric field in strengthening the interaction between the polar molecule groups and the graphene layer, leading to the distortion and expanding of graphene layer. This is a universal and highly efficient strategy to modify various hard carbons within minutes. The optimized hard carbon anode exhibits exceptional rate capability and cycling stability with a high retention rate of 88.4% after 15,000 cycles at 10C in ether electrolyte. It also displays remarkably improved reversible capacity, initial Coulombic efficiency ICE of 89.5% and cycling stability in ester electrolyte. It is revealed by in-situ electrochemical impedance spectroscopy and atomic force microscopy that the spontaneous formation of a thin, stable and inorganic substance-rich solid electrolyte interface layer with significantly improved mechanical property is largely responsible for the outstanding sodium-ion transport kinetics and long lifespan.

1. Introduction

Electrochemical energy storage technology has been playing an increasingly important role since the main countries in the word put forward the goals of “carbon peak” and “carbon neutrality”. As a representative, lithium ion batteries (LIBs) have expanded relatively maturely. However, with the rapid evolution of portable electronic devices and new energy power vehicles and the continuous growth of market demand, the global mineral products about lithium, cobalt, nickel resources will not be able to meet the requirement, which will eventually obstruct the further development of new energy industry [1,2]. Therefore, the market urgently needs to develop a new energy storage system with high safety, rich resources, wide distribution, environmentally friendly and suitable for large-scale applications to supplement and partially replace LIBs, and sodium ion batteries (SIBs) have attracted widespread attention [3,4]. Electrode materials, as the main body of sodium storage in batteries have been studied and achieved satisfactory performance in cathodes such as layered oxides [5,6], polyanionic compounds [7,8] and Prussian blue [9,10], etc. Now, anode materials bottleneck hinders the advancement of SIBs.

At present, research on anodes mainly focuses on carbon based materials [11,12], alloys [13,14], transition metal oxides [15,16] and organic compounds [17,18]. Among them, hard carbon is considered the most full-fledged and commercially viable anode material due to its high theoretical capacity, diverse structure, low cost, good conductivity, small volume deformation after sodium insertion and low redox potential [19]. The only fly in the ointment is the fact that hard carbon also has some drawbacks, such as low initial Coulombic efficiency (ICE), unsatisfied rate performance, insufficient long cycle stability and different performance depends on precursor selection and treatment methods, inevitably restrict its practical development. Especially in the commercial low-cost ester electrolyte, hard carbon with abundant

* Corresponding author.
E-mail address: zshong@fjnu.edu.cn (Z. Hong).

https://doi.org/10.1016/j.cej.2024.154103
Received 24 April 2024; Received in revised form 8 July 2024; Accepted 16 July 2024
Available online 22 July 2024

defects tends to form uneven, thick, mechanically weak, and easily fractured solid electrolyte interface (SEI), resulting in its performance in ester is far weaker than that in ether electrolyte [20,21]. To this end, researchers have made tremendous efforts, including reasonable control of hard carbon defect and interlayer spacing [22–24], regulation of pore structure [25–28], optimization of oxygen-containing functional groups [29,30], composite of soft and hard carbon to improve conductivity [31], selection of suitable electrolyte system [32,33], and construction of efficient and stable SEI [34,35] to enhance the performance of hard carbon.

However, most of these methods are complex to operate, costly, time-consuming and result in significant energy consumption. Nowadays, Joule heating technology, as a promising emerging sintering way, is used to instantaneously synthesize or change the structure of materials by means of external electric field regulation [36–38], which greatly saves time and cost. For example, Tour et al. reported a flash Joule heating method to quickly obtain a high temperature over 3000 K, achieving rapid synthesis of gram-weight graphene [21]. Huang et al. observed in real time that amorphous carbon nanowires formed tubular structures on the surface and nano onion-like structures inside under high bias Joule heating through high-resolution transmission electron microscopy (HRTEM), demonstrating the distortion of graphene layer by this route [39]. More recently, our group reported ultrafast synthesis of hard carbon for the first time by using spark plasma sintering (SPS) technology [40], which is generally used to synthesize alloys, ceramics and graphene, etc., with very little reports in the field of hard carbon materials. Herein, we make a further extension, utilizing Joule heating of such technology to reconstruct and modify the structure and composition of the pristine hard carbon. Under the fast post-treatment of such route within several minutes, the microstructure of hard carbon transformed into highly disordered vortex layer structure composed of thin and curved graphite-like domains. We tested the electrochemical performance of hard carbon in different electrolytes, and found that the remarkably improvement in capacity, rate performance, and cycling stability at high rates. In ether electrolyte, the retention rate can reach 88.4 % after 15,000 cycles at 10C with decay rate per cycle is only 0.0008 %. And in ester electrolyte, the reversible capacity increased from 295.3 to 342.3 mAh g^{-1} with a 21 % increase in low-pressure plateau capacity, and a significantly improved in cycling stability. In addition, we conducted a detailed investigation into the interface electrochemistry of the electrode and found that the SEI film of the reconstructed hard carbon is thinner, more uniform, and has a higher content of inorganic components.

2. Experimental section

Materials synthesis. Firstly, the commercial hard carbon spheres (ATEC, Japan) as raw material to be treated by the Joule heating in a SPS furnace. Specifically, after drying the raw materials, take an appropriate amount and place it in the graphite mold at a heating rate of 100 ~ 120 ℃ min^{-1}. After arriving at the target temperature (800, 1000, 1200 ℃), the heating time was held for 5 min. During this process, apply the voltage of 3 ~ 4 V, the current of ~ 500 A, the output power of 1.5 ~ 2 KW and the pressure of 25 MPa. The obtained hard carbon samples are labeled as HC-S800, HC-S1000, and HC-S1200, respectively. After cooling the instrument to room temperature, remove the block shaped sample and grind it to obtain black powder. As a comparison, the hard carbon was heated in a tube furnace at 1000 ℃ for 1 h to verify the effect of applying only a thermal field and labeled HC-T1000. In addition, CHC-S1200 and Kuraray-S1200 were prepared using corn starch based and Japanese Kuraray hard carbon as raw materials by the same process as ATEC hard carbon.

3. Results and discussion

3.1. Morphological and structural characterization

The structural reconstruction strategy is realized by taking typical spherical hard carbon as raw material and applying biased Joule heating in a SPS furnace with a very fast heating rate and short keeping time. The schematic diagrams are shown in Fig. 1a and S1a-c, the hard carbon obtained at different temperatures is labeled as HC-SX (X represents temperature) respectively. Additionally, the contrastive hard carbon heated at 1000 ℃ in a common tube furnace with only thermal field is labeled HC-T1000. Specifically, the structure of hard carbon is greatly improved under the multifield heating integrating by electric, thermal and pressure field. Scanning electron microscope (SEM) images (Fig. 1c and S2) show that, unlike the clear granular morphology accompanied some debris of HC and HC-T1000, the carbon spheres of HC-SX all exhibit the shape of mutual adhesion, similar to “cooked rice dumpling”, and the debris particles are once again melted into the sphere, and the higher the temperature, the more obvious the melting effect. HRTEM (Fig. 1d–h) is further utilized to observe the microstructure of the samples, and it is found that pristine HC is composed of thick and numerous short-range ordered graphene layers. The thickness of HC-T1000 after tube furnace treatment is reduced, and the disordered degree is increased slightly. However, the HC-SX treated with SPS manifest the vortex layer structure composed of thin and locally twisted graphite-like domains. With the increase of temperature, the degree of curvature become more pronounced, and the length of graphite-like domains increase. We perform ab initio molecular dynamics (AIMD) simulation and differential charge density distribution (DCDD) to explore the formation mechanism under the multifield reaction (Fig. 1b and S1d), and the specific parameters can be found in the supplement information. The AIMD result demonstrates that the parallelly stacked graphene layer greatly distort after conducting 6 fs under multifield heating condition. In addition, the theoretical simulation demonstrates the interlayer spacing increasement from 0.385 nm for the initial configuration to 0.399 nm for the final state. Considering the weak effect of thermal field, so we speculate the additional electric field plays the crucial effect on the structure change through the following aspects: 1) The electric field induced polarity effects in the ketone and hydroxyl groups, in which the oxygen atoms are affected by the polarity of the electric field, possibly leading to the displacement of the electron cloud, thus causing deformation of the entire molecular layer. 2) The electric field may lead to the redistribution of electrons, resulting in local charge inhomogeneity. This can induce graphene layer to deform under the action of an electric field to adapt to the new charge distribution. 3) There may be an interaction between the ketone and hydroxyl groups and the graphene layer, and the electric field strengthens this interaction, promoting distortion of the molecular structure. This suggestion is verified by the DCDD calculations of C=O and C-OH groups under electric field, as revealed from Fig. 1a and Fig. S1d. The electric field strengthens the interaction between the ketone and hydroxyl groups and the graphene layer with stronger charge transfer, promoting distortion of the molecular structure in order to achieve new charge distribution. Indeed, it is found from the HRTEM images that the interlayer spacing (d_{002}) of the reconstructed hard carbons have also increased. Concretely, the d_{002} of HC is 0.385 nm, while the d_{002} of HC-S1000 is 0.395 nm. When the post-treatment temperature increases to 1200℃ (HC-S1200), it still keeps remarkable curvature structure with more graphite-like microcrystalline stripes, though the interlayer spacing nearly converts back.

This phenomenon is also confirmed by the X-ray diffraction (XRD) spectra shown in Fig. 2a, which are typical of hard carbon with two broad peaks at ~ 22° and ~ 43°, corresponding to the (0 0 2) and (1 0 0) crystal planes of disordered carbon. The R factor is used to measure the degree of graphitization of hard carbon samples. From Fig. S3, the R value of HC is 2.19, and that of HC-S800, HC-S1000 and HC-S1200 are 1.50, 1.40 and 1.88 respectively. The smaller the R factor, the lower the

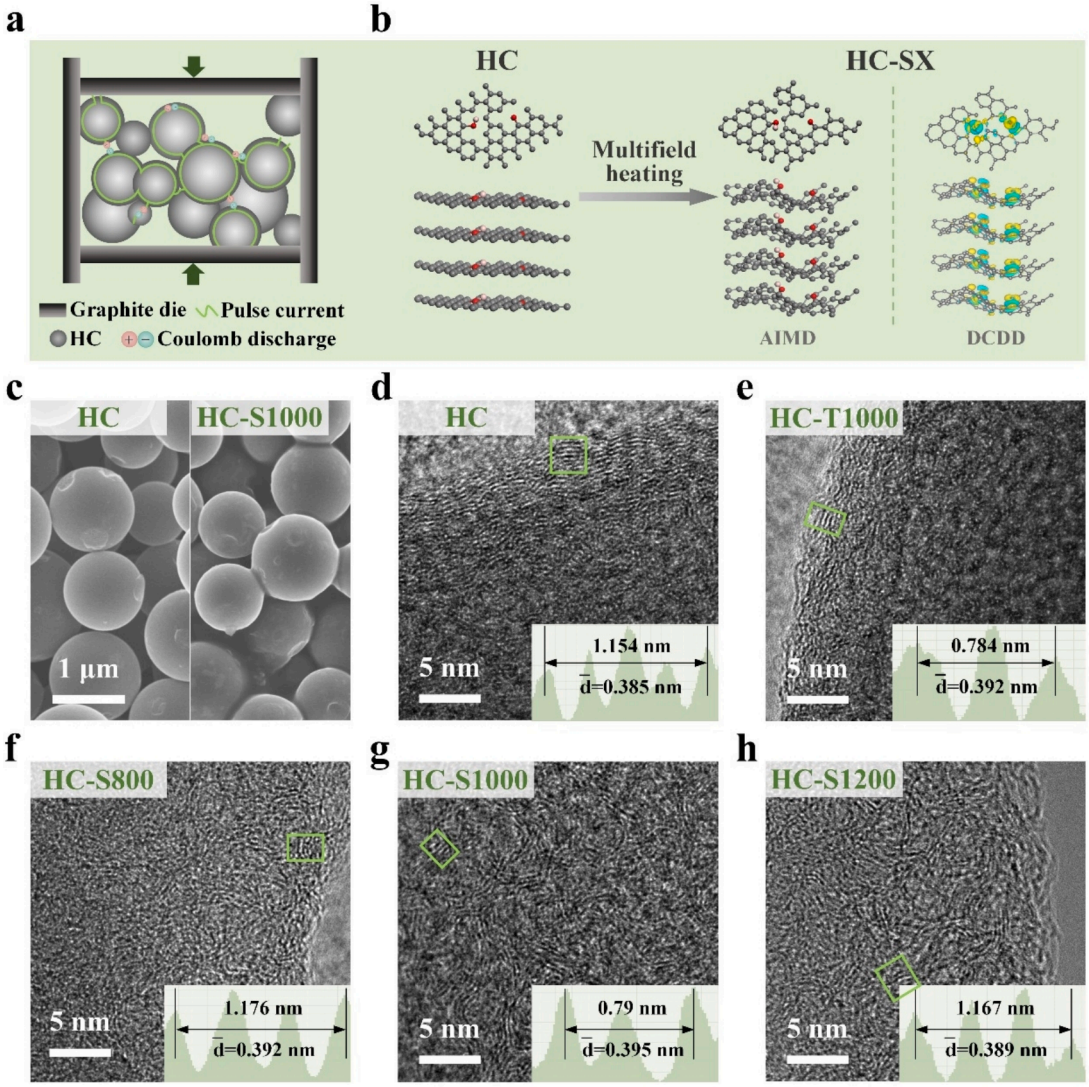

Fig. 1. (a) The schematic diagram of the heating mechanism for the sintering process, (b) ab initio molecular dynamics (AIMD) simulation of the sintering process and the differential charge density distribution (DCDD) which show the side and top view of graphene layer with C=O and C-OH group, (c) SEM and (d-h) TEM images of HC, HC-T1000, HC-S800, HC-S1000 and HC-S1200.

degree of graphitization and the more disordered the structure [41]. Raman spectroscopy was applied to further analyze the structure and confirm this result. As shown in Fig. 2c, the Raman spectra of the four samples have two characteristic bands near 1350 cm^{-1} (D-band) and 1580 cm^{-1} (G-band), which are derived from the vibration models of disordered and ordered carbon atoms individually [30]. In order to reveal the exact differences between these samples in depth, the D-band was further subdivided into D_1 (1350 cm^{-1}), D_2 (1610 cm^{-1}), D_3 (1490 cm^{-1}), and D_4 (1200 cm^{-1}) bands. The intensity ratio between D_1 band (I_{D_1}) and G band (I_G) is usually used to investigate the disorder degree of carbon materials [42]. The I_{D_1}/I_G of HC, HC-S800, HC-S1000 and HC-S1200 are 1.12, 1.39, 1.49 and 1.15, respectively. It is an almost universal recognition that the higher the carbonization temperature, the fewer defects and the higher the degree of graphitization, resulting in a lower strength ratio of I_{D_1}/I_G. However, the I_{D_1}/I_G value magnifies with the increase of pyrolysis temperature, which may be due to the formation of quasi closed pores in the bent carbon layers, which affects the degree of disorder value [26]. This result is in accordance with the HRTEM and XRD results. The surface chemical composition of the samples was determined by X-ray photoelectron spectroscopy (XPS). As can be seen from Fig. 2b, the materials are composed of C and O. After SPS post-treatment, for the sake of thermal and electric field effects, the oxygen functional groups decompose, resulting in the reduction of oxygen content. The high-resolution O1s spectra of the samples (Fig. S4) are mainly derived from C-O (533.9 eV) and C=O (532.5 eV) [43]. As the temperature rises, the proportion of C-O groups gradually decreases, while the proportion of C=O groups with better electrolyte affinity gradually increases (Table S1), which will facilitate the transport of sodium ions and stabilize the electrode/electrolyte interface [44]. The pore structure of samples was studied by N_2 (77 K) adsorption/desorption isotherms. As shown in Fig. 2d and e, the four samples exhibit typical type IV isotherms with lots of pores [45]. The specific surface areas (S_{BET,N_2}) of HC, HC-S800, HC-S1000 and HC-S1200 are 47.21, 19.60, 11.54 and 8.65 m^2/g, respectively, indicating a remarkably downward trend after post-treatment due to the reduction of open pores. The lower S_{BET,N_2} can reduce the side reactions between the hard carbon material and the electrolyte, thus reducing the formation of SEI, contributing to improve ICE. Meanwhile, the pore size distribution is mainly concentrated at 2 ~ 8 nm, and the pore volume decreases gradually with the ascension of treated temperature. This evolution of pore size can be attributed to the reduction of functional groups at higher sintering temperature and the stronger stacking interaction between the graphite-like domains [46]. Owing to the better diffusion ability of CO_2 at 273 K compared to N_2 at 77 K, CO_2 adsorption/

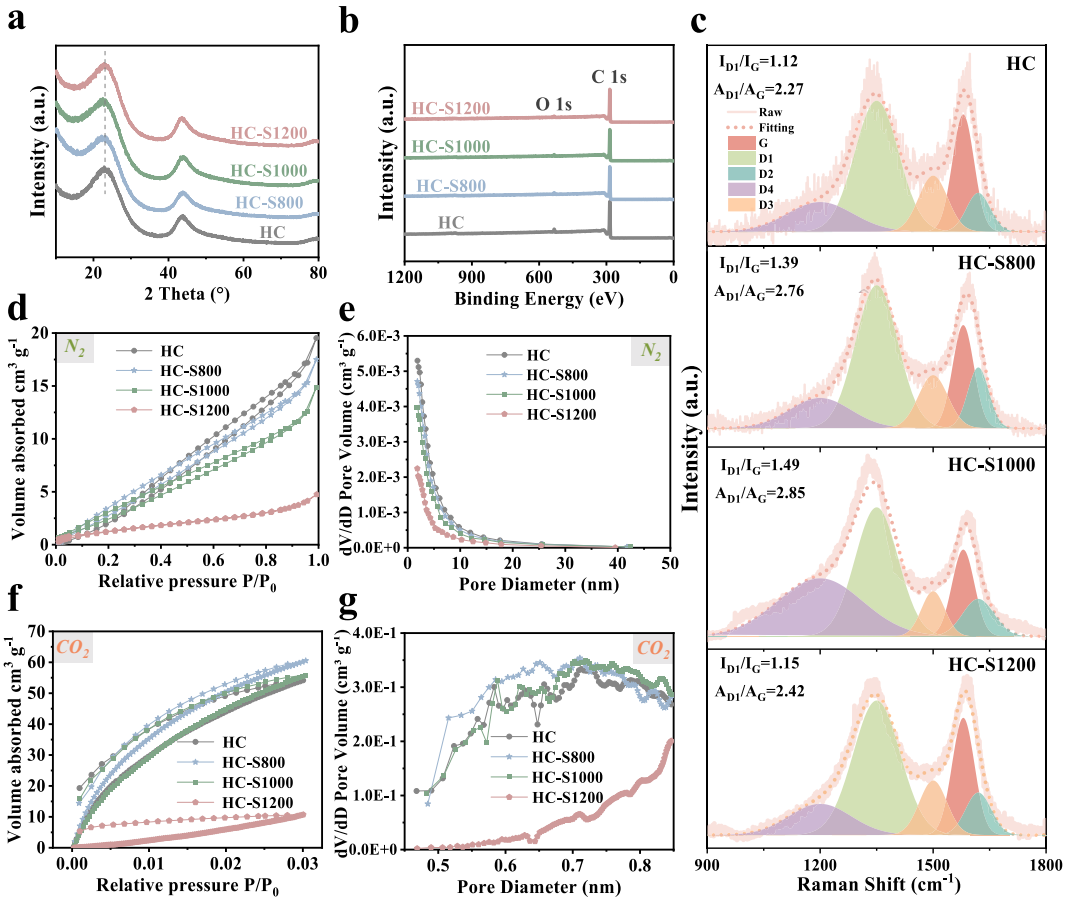

Fig. 2. Structural characterizations of HC and HC-SX. (a) XRD patterns, (b) XPS spectra, (c) Raman spectra fitted by Gaussian function, (d, e) N_2 and (f, g) CO_2 adsorption/desorption isotherms and the corresponding pore size distribution curves.

desorption measurements are took to study ultra-micropores in hard carbon samples. According to the aperture distribution curve (Fig. 2g), the ultra-micropores of the samples are concentrated in the pore size range of 0.6 ~ 0.8 nm, and the S_{BET,CO_2} of HC, HC-S800, HC-S1000 and HC-S1200 are 376.34, 476.81, 440.09 and 30.27 m^2/g, respectively (Fig. 2f). Accordingly, the volume of ultra-micropores increases from 0.1451 $cm^3 g^{-1}$ of HC to 0.1882 $cm^3 g^{-1}$ of HC-S800 and 0.1752 $cm^3 g^{-1}$ of HC-S1000, and goes down sharply to 0.0110 $cm^3 g^{-1}$ at 1200 ℃. The detail structural and compositional analysis are listed in Table 1. This result suggests that the content of ultra-micropores would increase after post-treatment at relatively low temperature, but it will decrease at too high temperature. In other words, this tendency also indicates the evolutionary process from open pores to close pores under this treatment, which will be verified from the sodium storage capacity in the following part.

3.2. Electrochemical performance and sodium storage mechanism

In order to investigate the sodium ions storage performance of the materials, all samples were assembled into half cells, and their electrochemical performance was tested briefly in ether (diglyme) electrolyte. The results are shown in Fig. 3a, exhibiting two regions, namely the plateau capacity region below 0.1 V and the slope capacity region above 0.1 V. HC-S1200 displays a reversible capacity of 340.9 mAh g^{-1} at 0.1C (1C=300 mA g^{-1}), along with an ultra-high ICE of 92.0 %, suggesting the remarkable capacity improvement. Fig. 3b reveals the proportion of plateau and slope capacity. Among them, HC-S1000 has the largest interlayer spacing and the highest ID1/IG, corresponding to the rich defects and more disordered structure, which can generate higher slope capacity. Nevertheless, the proportion of slope capacity decreases for HC-S1200 obtained at higher temperature (HC-S1200), as the reduction of specific surface area, oxygen content, and the defects. Meanwhile, HC-S1200 has a highest overall capacity due to the significant increased capacity in the plateau area. The previous studies have shown hard carbon anode exhibits undetectable or very thin SEI in ether electrolyte [35], leading to the improved sodium ion transport kinetics at the interface. As for the present rate performance test (Fig. 3c and S5) at 0.1, 0.2, 0.5, 1, 2, 3, 5 and 10C, it is found that HC-SX exhibit excellent and better rate performance, the differences in capacity between HC-SX and HC began to be prominent when the current density increased to 2C.

Table 1
Structural parameters of HC and HC-SX.

Sample	XRD		Raman	XPS		N_2 adsorption		CO_2 adsorption	
	d_{002} (Å)	R	I_{D1}/I_G	C (at %)	O (at %)	S_{BET} (m^2/g)	V_{pore} ($cm^3 g^{-1}$)	S_{BET} (m^2/g)	V_{pore} ($cm^3 g^{-1}$)
HC	3.85	2.19	1.12	96.21	3.79	47.21	0.0302	376.34	0.1451
HC-S800	3.92	1.50	1.39	97.43	2.57	19.60	0.0271	476.81	0.1882
HC-S1000	3.95	1.40	1.49	97.71	2.29	11.54	0.0122	440.09	0.1752
HC-S1200	3.88	1.88	1.15	98.12	1.88	8.65	0.0114	30.27	0.0110

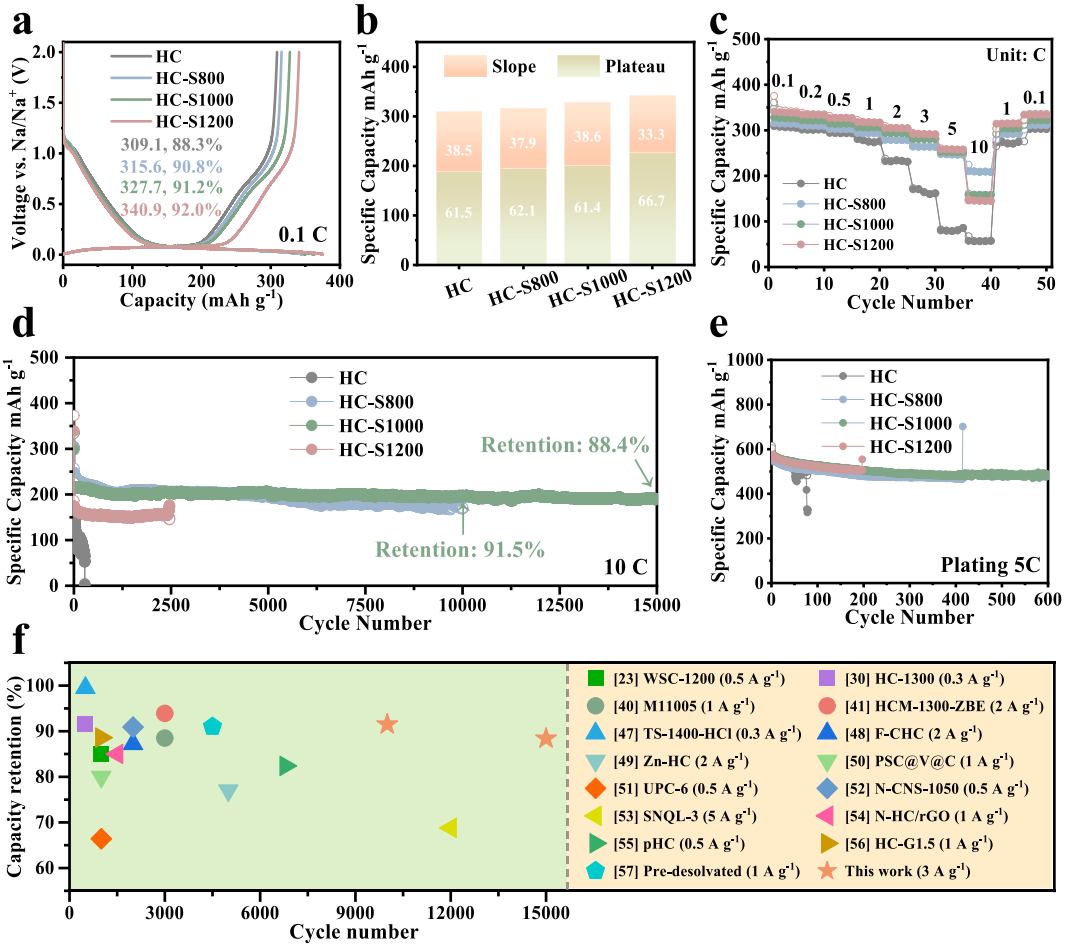

Fig. 3. Electrochemical performance of HC and HC-SX half cells in ether electrolyte. (a) The discharge and charge curves at 0.1C (1C=300 mAh g^{-1}) at the first cycle, (b) the contribution ratios of slope and plateau capacity, (c) rate capability, (d) long cycling stability at a high rate of 10C. (e) The cycling performance under overpotential state with a plating capacity of 300 mAh g^{-1} at 5C, (f) the comparative cycling stability and capacity retention ratios of hard carbons in the cited references.

Notably, the capacity of HC-S800 (210.2 mAh g^{-1}), HC-S1000 (157.5 mAh g^{-1}) and HC-S1200 (145.8 mAh g^{-1}) is 3.7, 2.7, and 2.5 times higher than those of HC (57.5 mAh g^{-1}) at 10C, respectively. It cannot be ignored that in terms of long cycling performance (Fig. 3d), HC stopped working after 280 cycles, while HC-S1000 can still achieve retention ratios of 91.5 % and 88.4 % after 10,000 and 15,000 cycles at 10C (activated with 1C in the first cycle), with a decay rate of only 0.0008 % per cycle, which is one of the best life-span and rate capability in the state-of-art hard carbon anode (Fig. 3f) [23,30,40,41,47–57]. The low plateau voltage of hard carbon anode inevitably produces the safe concern of sodium metal plating at a high charging rate in the practical application. Unexpectedly, HC-SX display much improved cycling stability under overpotential state (Fig. 3e and S6). HC can only work about 80 cycles, while HC-S1000 remains totally stable after 600 cycles at a high rate of 5C with a sodium plating capacity of 300 mAh g^{-1}. This result further verifies the incredible cycling performance of the modified hard carbon material which even can allow the partial electroplating at overpotential state.

Afterwards, we further measured the electrochemical performance of four electrodes in typical commercial ester electrolyte (EC/DMC/EMC) to demonstrate the superiority of the reconstructed hard carbon. The first discharge and charge curves of the electrodes at a current density of 0.1C are shown in Fig. 4a, as a commercial anode, the reversible capacity and the ICE of HC itself are 295.3 mAh g^{-1} and 84.7 %. After post-treatment, HC-SX has improved in different amplitude, specifically for HC-S800 (311.8 mAh g^{-1}, 85.6 %), HC-S1000 (326.9 mAh g^{-1}, 87.7 %), and HC-S1200 (342.3 mAh g^{-1}, 89.5 %). The corresponding contribution rates of plateau and slope capacity can be seen in Fig. 4b, compared to HC, the capacity of HC-SX at both two regions has been improved. Specifically, similar to that in ether electrolyte, HC-S1000 exhibits the highest slope capacity, while the capacity improvement of HC-S1200 mainly comes from the plateau region, with a plateau capacity of up to 213.5 mAh g^{-1}, which is about 21 % higher than HC. This represents the formation of more close pores, corresponding to the above structural analysis. Fig. 4c and S7 show the capacity of the electrodes at different rates (0.1–0.2–0.5–1–0.5–0.2–0.1C). It is noteworthy that although the capacity of HC-S800 is not significantly increased, it has the best rate capability, reaching 223.2 mAh g^{-1} at 1C, which is three times the capacity of HC under the same conditions. This is because it simultaneously has abundant pores and disordered structure. In the meantime, the rate performance of HC-S1000 is also relatively good. Next, we tested the cycling performance of the electrodes at 0.2C (Fig. 4d) and 0.1C (Fig. 4e), respectively. It is shown that the capacity retention ratio of HC is only 41.3 % after 50 cycles, while HC-SX have been greatly enhanced, and HC-S1000 displays the best cycling stability with 79.8 % retention. And the same is true under the condition of 0.1C, HC-S1000 can still attain a retention ratio of 82.3 % after 90 cycles, an increase of 31.4 % compared with HC. The research has shown that the stored sodium in the plateau area is quasi-metallic sodium, it is not easy to stabilize in HC and will easily produce capacity fading with too high plateau capacity [11]. In order to verify the capability of the prepared hard carbon materials to accommodate quasi-metallic sodium, we

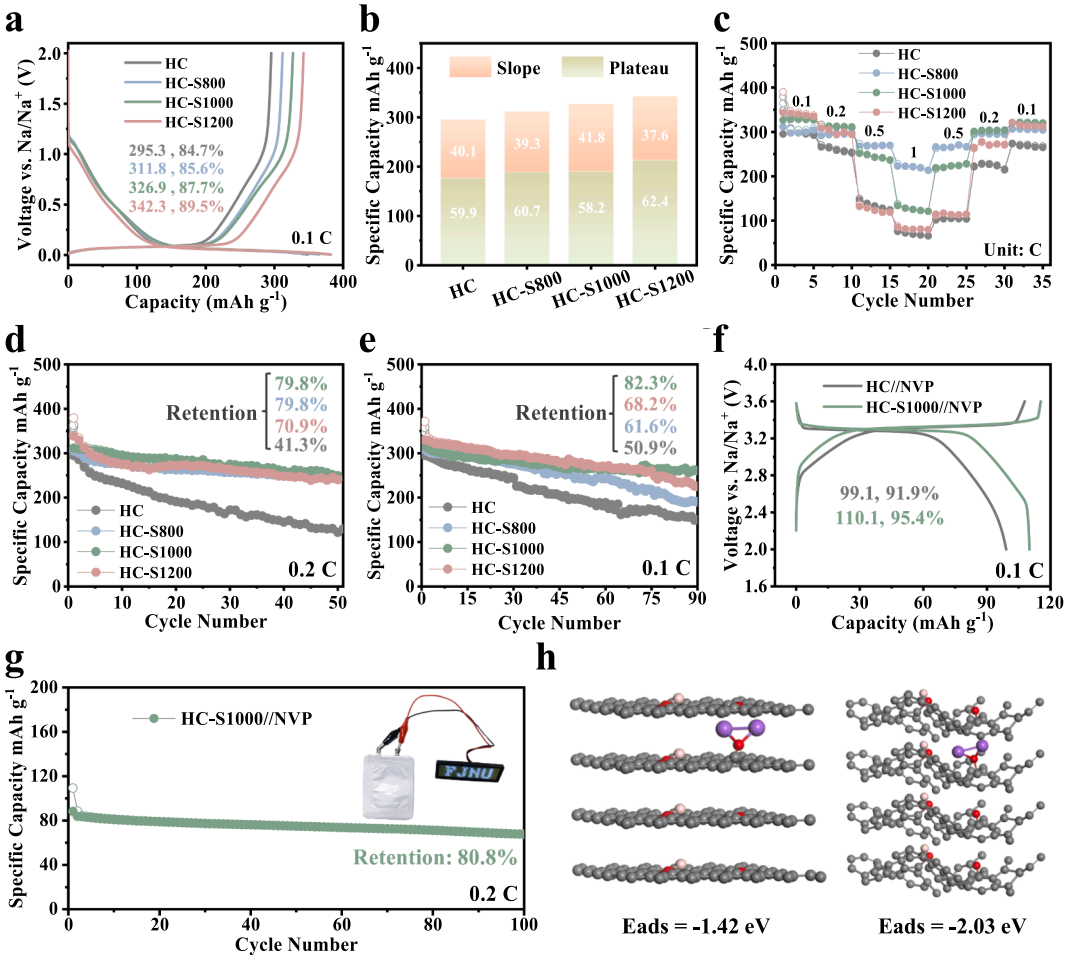

Fig. 4. Electrochemical performance in ester electrolyte. (a) First cycle discharge and charge curves, (b) contribution ratios of slope and plateau capacity, (c) rate capacity and (d, e) cycling performance of HC and HC-SX half cells. (f) First cycle charge and discharge curves of HC//NVP and HC-S1000//NVP coin full cell and (g) cycling performance of HC-S1000//NVP pouch full cell. (h) The adsorption energy of metallic sodium with two-atom aggregates on HC (left) and HC-SX (right) materials.

calculated the adsorption energy of metallic sodium on such two different materials. As shown in Fig. 4h, it is found that the adsorption energy of HC-SX-Na was −2.03 eV, which is about 0.61 eV lower than that on HC-Na (−1.42 eV). In other words, the storage of metallic sodium aggregates in the HC-SX structure can be more stable, which helps to improve the stability of the material in the plateau region and thus enhance the overall cycling performance of the material [58]. To summarize, the ICE and cycling stability of HC anode in ester electrolytes are significantly improved by the fast post-treatment with Joule heating. Although the overall performance in ester electrolytes is not as good as in ether electrolytes, it is common in the previous study [33], and the detail reason will be discussed below.

Meanwhile, so as to explore the respective roles of pressure, thermal and electric field in more detail, we prepared HC-S1000-2P (Fig. S8) obtained by post-treatment with SPS under double pressure (50 MPa), and the results show that its performance is very close to that of HC-S1000 in all aspects. Then, we further investigate the performance of HC-T1000 sample derived by post-treatment with a tube furnace with only thermal field at the same temperature, as shown in Fig. S9, it is found that the improvement in reversible capacity, rate performance, and cycling ability is negligible compared to HC and far inferior to HC-S1000, indicating that electric field plays a crucial important role in this multi-field sintering process. Finally, for the sake of confirming the universality and applicability of Jouel heating post-treatment to hard carbon materials ulteriorly, we also make use of this technology to sinter corn starch based and Kuraray hard carbon under the above optimized conditions, and its electrochemical performance is exhibited in Fig. S10. As for corn starch based hard carbon (CHC) prepared from our previous work [59], the reversible capacity is remarkably improved from 296.2 to 320.2 mAh g^{-1}. While for the hard carbon from Kuraray, its rate capability has been obviously enhanced. At 0.5C, Kuraray-S1200 has a reversible capacity of 237.7 mAh g^{-1}, which is more than two times than the pristine sample of 106.3 mAh g^{-1}. The commonality between the two samples is that there is a significant improvement in cycle stability, as evidenced from 53.5 % to 93.0 % retention for CHC and from 48.5 % to 82.7 % for Kuraray after 50 cycles at 0.2C.

To estimate the practical application potential of hard carbon materials, we have assembled full cells by using HC and HC-S1000 as the anodes and $Na_3V(PO_4)_3$ (NVP) as the cathode in ester electrolyte, and as a supplement, the performance of NVP half cells were also tested. It has to mention that it is not very reliable to obtain the true capacity of electrode materials from half-cell test in easter electrolytes due to interference of metallic sodium electrode in SIBs [60]. It is revealed the overpotential and impedance of the metallic sodium electrode in ester electrolyte are much higher than those in ether electrolyte, resulting in more underestimation of capacity [20], which has been widely confirmed in the studies of various types of cathode/anode materials [32,33,61,62]. This is the main reason that the half cells test in ester electrolytes (Fig. S11a-c) can not obtain the real capacity of NVP cathode, but its capacity can be fully released in ether electrolytes (Fig. S11a-c). In addition, Li et al. [63] have demonstrated that the electrode displayed higher ICE and better rate performance in full cells compared to

half cells due to the absence of sodium electrode interference. Therefore, comparing the electrochemical performance of HC//NVP and HC-S1000//NVP full cells is more valuable. As shown in Fig. 4f, HC-S1000//NVP provides a high reversible capacity of 110.1 mAh g^{-1} and an ultra-high ICE of 95.4 % at 0.1C based on the mass of the cathode electrode in coin full cells, however, the performance of HC//NVP is unsatisfactory, with a capacity of 99.1 mAh g^{-1} and an ICE of 91.9 %. Accordingly, HC-S1000//NVP delivers a higher energy density of 267 Wh kg^{-1}compared with HC//NVP of 237 Wh kg^{-1} based on the entire mass of active materials. Fig. S12a shows their rate performance at 0.1, 0.2, 0.5, 1.0, and 2.0C, delivering the reversible capacity of 99.1, 82.3, 74.1, 69.1, and 64.5 mAh g^{-1} of HC//NVP and 110.1, 102.1, 94.4, 90.2, and 86.6 mAh g^{-1} of HC-S1000//NVP, respectively. Such rate performance is better than that in the half cells, suggesting that it can't obtain the true rate capability of anode/cathode materials by half-cell test due to the large polarization of metallic sodium in ester electrolyte. Further testing was conducted on the cycling stability and service life of the HC//NVP and HC-S1000//NVP coin full cells at 1C, as shown in Fig. S12b. After 150 and 300cycles, the capacity retention ratios of HC//NVP were only 34 % and 19 %, while those in HC-S1000//NVP can achieve 80 % and 70 %, demonstrating good durability and stability. The pouch full cells achieving with a high energy density of 217.7 Wh kg^{-1} (the detailed parameters can be found in Table S2) further highlights the excellent performance of HC-S1000 (Fig. 4g), which can remain an 80.8 % retention after 100cycles at 0.2C and also can lighten a LED light. The results based on full cells strongly indicate that HC-S1000 has taken all aspects of performance to the next level on the basis of HC.

3.3. Sodium storage mechanism and interface electrochemistry

CV, GITT, and in-situ electrochemical impedance spectroscopy (EIS) methods are utilized to evaluate the storage dynamics of sodium ions and the property of SEI film, and the above tests are all based on electrodes in ester electrolyte. Fig. S13 shows the initial three-cycle CV curves for the four electrodes at a scanning rate of 0.1 mV/s. A pair of reversible redox peaks appear near 0.005 and 0.15 V, corresponding to the insertion/extraction of sodium ions in the carbon framework [50]. During the first scanning, two irreversible broad peaks appeared between 0.4 and 1.2 V, mainly due to the formation of SEI layers caused by electrolyte decomposition [64]. It is obvious that the irreversible broad peak of HC-SX at the first cycle is smaller than that of HC, indicating that less irreversible decomposition of electrolyte occurs on the surface of HC-SX, which facilitate the formation the thin SEI layer. At a deeper level, CV curves at different scanning speeds (0.2–0.5–1-2 mV/s) are studied (Fig. 5a–d), and it is found that with the increase of scanning rate, the oxidation peak shift slightly towards the high potential, indicating a slight polarization of the electrode. It is demonstrated there is a power-law relationship between scanning rate (v) and peak current (i).

$$i = av^b \quad (1)$$

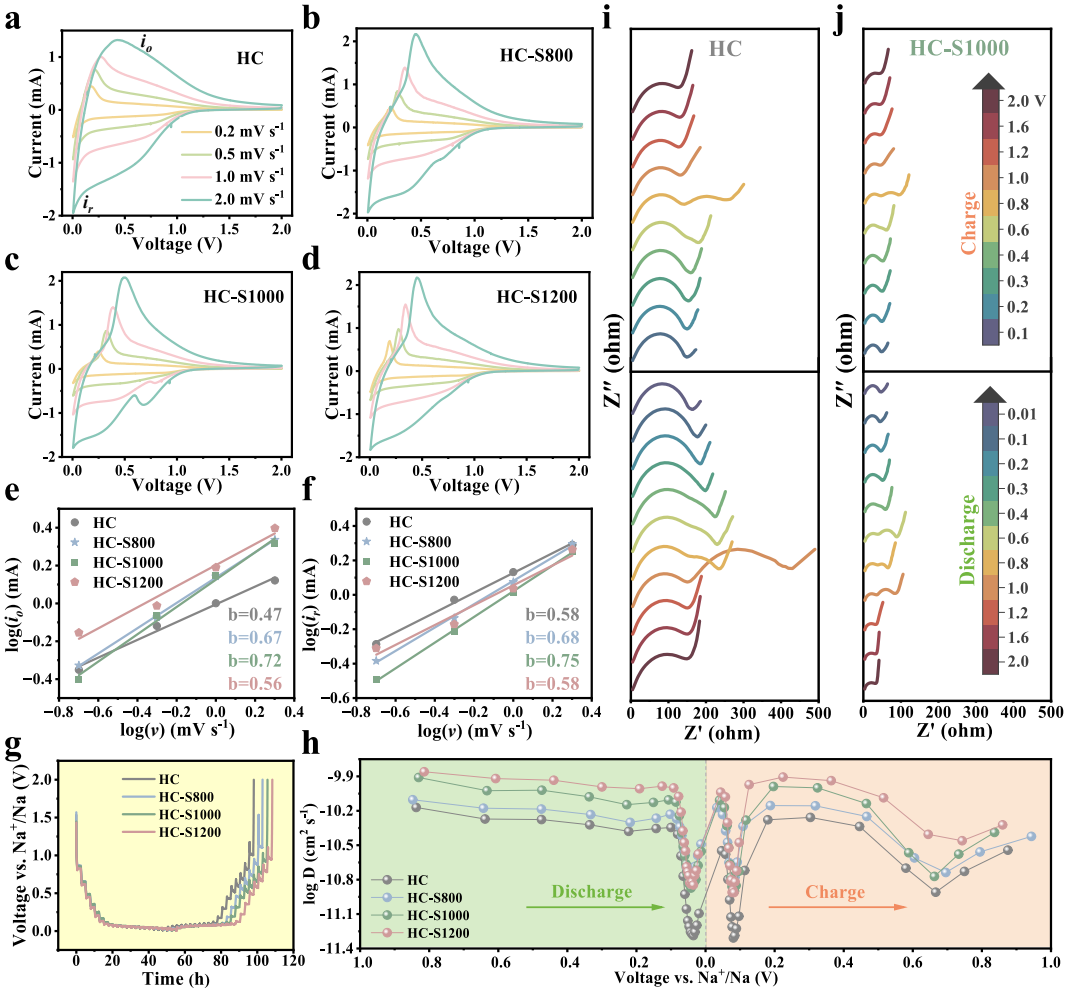

Fig. 5. Kinetic analysis of HC and HC-SX half cells in ester electrolyte. (a-d) CV curves at different scanning speeds, corresponding b values of (e) the oxidation and (f) reduction peaks, (g) GITT curves during the second discharge and charge process and (h) sodium ion apparent diffusion coefficients. In situ EIS of (i) HC and (j) HC-S1000 electrodes at different potentials during the first discharge and charge process.

where a and b are reaction correlation constants, and b values in different potential regions can reflect the storage behavior of sodium ions. Fig. 5e and f show the linear relationship between the two sharp oxidation and reduction peaks log $i_{o/r}$ and log v of all samples. The oxidation and reduction peaks b values of HC are 0.47 and 0.58, respectively, demonstrating that the storage of sodium ions is dominated by diffusion, which is considered to be the embedding of sodium ions in graphite-like domains and the filling of nanopores [65]. The b values of both oxidation and reduction peaks of HC-SX have increased, concretely manifested as 0.67 and 0.68 for HC-S800, 0.72 and 0.75 for HC-S1000, and 0.58 and 0.60 for HC-S1200, explicating an increase in the contribution of capacitive control processes with faster kinetics [66]. To further supplement, HC and HC-S1000 are selected as representatives, and a more detailed calculation is performed for them using the following formula [51].

$$i(v) = k_1 v + k_2 v^{1/2} \quad (2)$$

where $k_1 v$ and $k_2 v^{1/2}$ represent capacitance and diffusion controlled processes. Figs. S14 and 15 show that the capacitance contribution ratios of both of them increase with the increasing scan rate. When the scanning rate is 0.2, 0.5, 1.0 and 2.0 mV/s, the capacitance contribution of HC-1000 is 64 %, 70 %, 76 % and 85 % respectively, which is higher than that of HC at the same scanning rate. The higher capacitance contribution is beneficial to improve sodium storage kinetics, so the HC-S1000 anode exhibits better rate performance than HC. This variation trend agrees well with their intrinsic structure, suggesting that the structural reconstruction after post-treatment producing expanded interlayer spacing and the increased disordered degree boost the sodium ion transport ability.

Next, the dynamic characteristics of the electrodes were further revealed using GITT at the second discharge and charge (Fig. 5g and h). GITT showed that the sodium ions diffusion coefficient of HC-SX during was generally higher than that of HC, implying that HC-SX has faster diffusion kinetics. Finally, in situ EIS was measured for the electrodes in the first cycle (Fig. 5i and j and Table S3), and equivalent circuit fitting was performed on the obtained data. It is found that the overall ohmic resistance R_s of the HC anode was greater than that of the HC-S1000 anode, which should be due to the reduction of internal resistance after structural reconstruction. By tracking the SEI resistance (R_{SEI}) at different stages, it was observed that SEI began to form at 1.0 V on both electrodes, and the R_{SEI} value of HC increased visibly during low potential discharge, implying continuous electrolyte reduction and SEI accumulation. However, the R_{SEI} of HC-S1000 remained low and changed steadily during discharge process, illustrating that electrolyte reduction on the HC-S1000 anode was limited and SEI evolution was stable. Besides, the R_{ct} of HC-S1000 is also much smaller than HC generally during the whole discharge and charge process. A lower R_{SEI} value indicates a faster transport speed of sodium ions on SEI, which is the reason for the improved rate performance of the HC-S1000 anode [44]. At the same time, HC-S1000 still has the lowest impedance after 50 cycles (Fig. S16b), which verifies its lowest energy barrier at the interface and faster sodium ions transport kinetics.

In an effort to reveal the relationship between SEI and sodium storage behavior, XPS was used to study the structure and composition of the SEI layer before (0 s) and after (330 s) etching of the two electrodes of HC and HC-S1000 after 50 cycles (Fig. 6 and Table S4). Before etching, the C1s spectra can be divided into four peaks of 284.1 eV (Na_x-HC), 285.2 eV (C-C/C-H), 286.3 eV (C-O) and 289.1 eV (C=O), implying that the SEI film formed on both electrodes contains Na_x-HC, organic (CH_2OCO_2Na) and inorganic salts (Na_2CO_3) components [67]. The O1s peaks of 530.9 eV (C=O) and 533.0 eV (C-O) represent Na_2O, Na_2CO_3, and CH_2OCO_2Na, respectively. In addition, the O1s spectra show Na Auger electron peaks (535.9 eV), implying that most organic substances are sodium containing compounds. The spectral peak of Na 1 s for 1071.0 eV (Na-O/Na-F) corresponds to Na_2O and NaF. The peak of F 1 s, except for 684.4 eV (Na-F), corresponds to the residual Na_xPF_y at 686.4 eV (P-F) [20,68,69]. After etching for 330 s, it can be observed that the peaks of C and O representing organic components become weak, while the inorganic species of Na-O and Na-F peaks become stronger and sharper. These results showed that organic carbonates were primarily

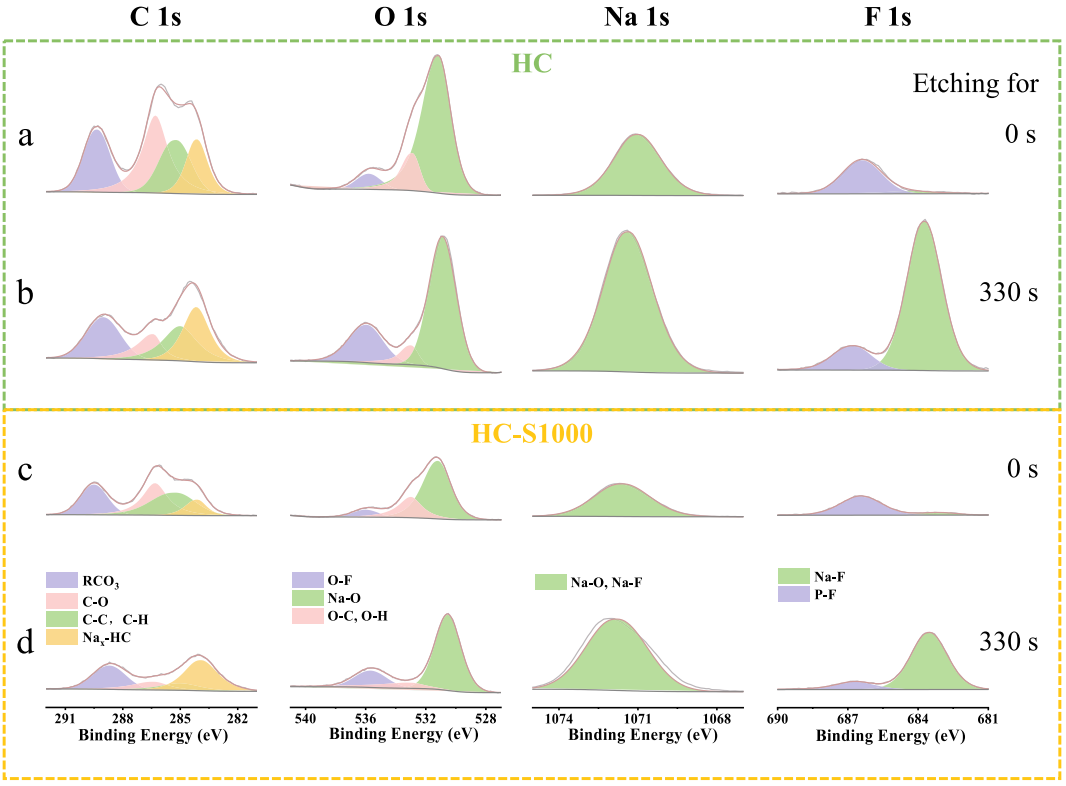

Fig. 6. XPS spectra before and after etching for (a, b) HC and (c, d) HC-S1000 electrodes after 50 cycles.

distributed in the outer layer of SEI, and inorganic substances such as Na_2CO_3, NaF and Na_2O were mainly distributed in the inner layer. Notably, the increase in the relative content of Na_x-HC on HC-S1000 electrode after etching (32.24 %) is much higher than that of HC (13.34 %), which is due to the thinner coverage of the SEI layer [70]. Moreover, the proportion of inorganic components in SEI on HC-S1000 anode is generally higher than that of HC, as mentioned earlier, rich inorganic components are beneficial to the construction of stable SEI with better uniformity, which contributes to the stability and excellent cycling performance of HC-S1000 anode. Besides, the inorganic component that penetrates the SEI has higher sodium ions conductivity than its organic component, which is the reason for the significant improvement in the anode rate performance of HC-S1000 [71].

Furthermore, to reveal the reason for such a big difference in cycling performance, SEM and the corresponding energy dispersive X-ray (EDX) mapping were applied to observe the morphology and structure of HC and HC-S1000 electrodes after 50 cycles, as can be seen in Fig. 7a and d and S17. The surface of HC electrode was covered by extensive and thick covering, while the morphology of HC-S1000 electrode remained intact, similar to the initial state. The EDX result reveals that HC-S1000 electrode has less surface O, Na, F, and P content than the HC electrode (Table S5). TEM image shows that the SEI layer on the surface of HC was relatively loose with a thickness of about 35.1 nm (Fig. 7b) which is easy to drop out after ultrasound. By contrast, HC-S1000 was uniformly distributed with a thickness of only 7.1 nm (Fig. 7e), which was conducive to faster interface sodium ions transport, higher ICE and

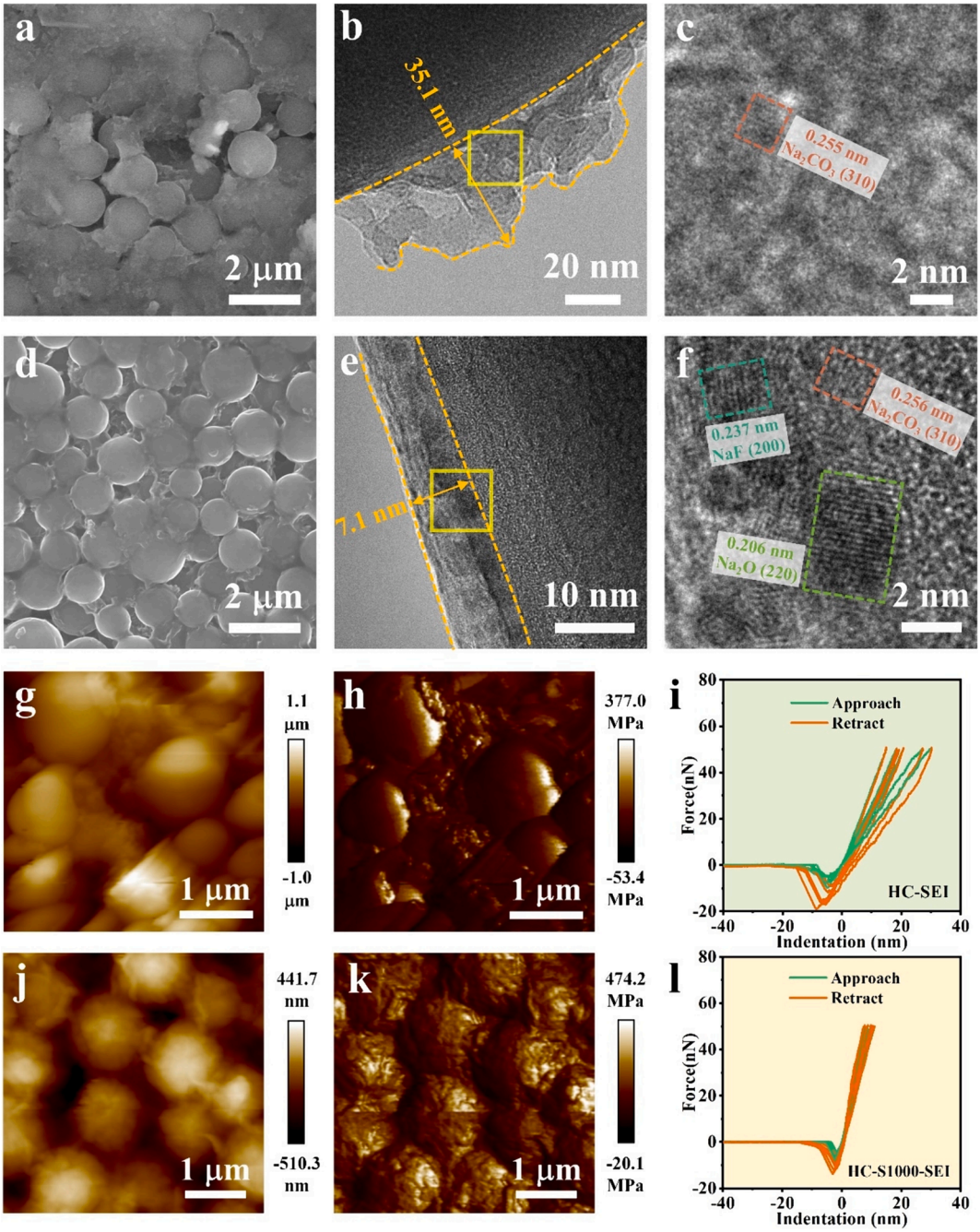

Fig. 7. (a, d) SEM, (b, e) TEM and (c, f) HRTEM images from the yellow solid line frames, (g, j) AFM height images, (h, k) the corresponding two-dimensional maps of elastic modulus and (i, l) representative force-indentation curves of selected sites for the formed SEI: (a-c, g-i) HC and (d-f, j-l) HC-S1000 electrodes after 50 cycles. (For interpretation of the references to colour in this figure legend, the reader is referred to the web version of this article.)

better rate capability. HRTEM images (Fig. 7c and f) show that the SEI layer of HC-S1000 electrode can be divided into an amorphous outer layer and a crystalline inorganic inner layer. There are some randomly distributed nanocrystals with lattice fringe distances of 0.206, 0.237 and 0.256 nm in the latter, corresponding to the (220) plane of Na_2O, the (200) plane of NaF, and the (310) plane of Na_2CO_3 [33,44]. The consequential EDX mapping of HC-S1000 electrode (Fig. S18) also confirms that its SEI film was mainly composed of Na, O, and F. It has been reported that the inorganic component has lower sodium ions diffusion activation energy (100–150 m eV) than the organic component [72], which effectively promotes the storage kinetics of sodium ions at the interface and improves the mechanical strength of the SEI layer.

The difference of SEI composition inevitably leads to the difference of mechanical properties, which has a great impact on interface and cycling stability. Therefore, the local mechanical properties of SEI formed on the HC and HC-S1000 electrodes after 50 cycles were measured with the help of atomic force microscopy (AFM). The typical spherical morphology of hard carbon is observed in Fig. 7g and j, where the carbon spheres of HC-S1000 are relatively uniform, while HC exhibit a rougher and more irregular morphology, accompanied by a large amount of electrolyte salts randomly distributed in the gaps between the carbon spheres, which is consistent with the observation results of SEM and TEM. In addition, the elastic moduli of the two electrodes are shown in Fig. 7h and k and S19. It can be obtained from the mapping that the Young's modulus obtained by the DMT model is higher for HC-S1000 (171.0 MPa) than HC (79.8 MPa). Seven sites focused on carbon spheres were selected from each mapping to study their mechanical performance, and the corresponding force–displacement curves were shown in Fig. 7i and l, under similar force loads, the SEI on the HC-S1000 electrode exhibits elastic deformation with small displacement, further demonstrating a higher modulus than the SEI formed on the HC electrode surface. In addition, the overlapped force curves of HC-S1000 between the approach and retract indicates the homogeneity of the SEI layer, while the HC electrode has a large deviation. The above results clearly show that the SEI of HC-S1000 electrode has excellent mechanical stability largely due to a higher proportion of inorganic substances [57,68], which can effectively protect the HC-S1000 electrode with a stable interface, thus greatly improving the Coulombic efficiency and cycling stability.

4. Conclusions

In summary, we first utilized Joule heating to the post-treatment of hard carbon enabling the structure reconstruction with improved disordered structure, expanding interlayer spacing due to the strong charge transfer under the electric field. The prepared hard carbon anode for SIB exbibits the ultrafast and ultra-stable sodium ion storage ability as well as good electrolyte compatibility. Firstly, HC-S1000 showed excellent high rate performance and incredible long cycle life with 88.4 % retention after 15,000 cycles at 10C in ether electrolyte, making it one of the most best anode materials reported so far. In ester electrolyte, the performance of HC-S1000 has been sensibly improved in ICE, rate capability and cycling stability. Furthermore, deep mechanistic studies have revealed the root reasons of rapid reaction kinetics and stable cycling due to the robust sodium ion transport performance in the bulk and at the interface. The formation of thin and inorganic substance-rich SEI layer with improved mechanical property is responsible for the enhanced sodium ion storage performance. Finally, the full cells composed of HC-S1000 anode and NVP cathode achieves high energy density and good cycling life, verifying its feasibility in practical applications. This work provides new insights into the structural modification and interfacial electrochemistry regulation of high-performance and practical hard carbon anodes.

CRediT authorship contribution statement

Ziqing Song: Writing – original draft, Investigation, Formal analysis. **Qiyan Du:** Formal analysis. **Jing Chen:** Formal analysis. **Jin Huang:** Formal analysis. **Yue Chen:** Formal analysis. **Lituo Zheng:** Formal analysis. **Zhigao Huang:** Formal analysis. **Hong Dai:** Formal analysis. **Zhensheng Hong:** Writing – review & editing, Supervision.

Declaration of competing interest

The authors declare the following financial interests/personal relationships which may be considered as potential competing interests: Zhensheng Hong reports financial support was provided by National Natural Science Foundation of China. If there are other authors, they declare that they have no known competing financial interests or personal relationships that could have appeared to influence the work reported in this paper.

Data availability

Data will be made available on request.

Acknowledgments

This work was financially supported by National Natural Science Foundation of China (NSFC 52374302 and 51874099), National Science Foundation of Fujian Province's Key Project (2021 J02031), Natural Science Foundation of Fujian Province (2023 J01518) and Education Department of Fujian Province (JAT210054). We also thank the support from the open fund from Academy of Carbon Neutrality of Fujian Normal University (TZH2022-06 and TZH2022-08), and the Undergraduate Training Programs for Innovation and Entrepreneurship (cxx1-2024363).

Appendix A. Supplementary data

Supplementary data to this article can be found online at https://doi.org/10.1016/j.cej.2024.154103.

References

[1] Y. Yang, C. Wu, X.X. He, J. Zhao, Z. Yang, L. Li, X. Wu, L. Li, S.L. Chou, Boosting the development of hard carbon for sodium-ion batteries: strategies to optimize the initial Coulombic efficiency, Adv. Funct. Mater. 34 (2023) 2302277, https://doi.org/10.1002/adfm.202302277.
[2] M. Liu, Y. Wang, F. Wu, Y. Bai, Y. Li, Y. Gong, X. Feng, Y. Li, X. Wang, C. Wu, Advances in carbon materials for sodium and potassium storage, Adv. Funct. Mater. 32 (2022) 2203117, https://doi.org/10.1002/adfm.202203117.
[3] Y. Chu, J. Zhang, Y. Zhang, Q. Li, Y. Jia, X. Dong, J. Xiao, Y. Tao, Q.H. Yang, Reconfiguring hard carbons with emerging sodium-ion batteries: a perspective, Adv. Mater. 35 (2023) 2212186, https://doi.org/10.1002/adma.202212186.
[4] F. Wang, Z. Jiang, Y. Zhang, Y. Zhang, J. Li, H. Wang, Y. Jiang, G. Xing, H. Liu, Y. Tang, Revitalizing Sodium-Ion Batteries via Controllable Microstructures and Advanced Electrolytes for Hard Carbon, eSci. 100181 (2023), https://doi.org/10.1016/j.esci.2023.100181.
[5] Q. Liu, Z. Hu, M. Chen, C. Zou, H. Jin, S. Wang, S.L. Chou, Y. Liu, S.X. Dou, The cathode choice for commercialization of sodium-ion batteries: layered transition metal oxides versus Prussian blue analogs, Adv. Funct. Mater. 30 (2020) 1909530, https://doi.org/10.1002/adfm.201909530.
[6] L. Zheng, J.C. Bennett, M.N. Obrovac, Stabilizing $NaCrO_2$ by sodium site doping with calcium, J. Electrochem. Soc. 166 (2019) A2058–A2064, https://doi.org/10.1149/2.1041910jes.
[7] Y. Cao, C. Yang, Y. Liu, X. Xia, D. Zhao, Y. Cao, H. Yang, J. Zhang, J. Lu, Y. Xia, A new polyanion $Na_3Fe_2(PO_4)P_2O_7$ cathode with high electrochemical performance for sodium-ion batteries, ACS Energy Lett. 5 (2020) 3788–3796, https://doi.org/10.1021/acsenergylett.0c01902.
[8] H. Li, M. Xu, Z. Zhang, Y. Lai, J. Ma, Engineering of polyanion type cathode materials for sodium-ion batteries: toward higher energy/power density, Adv. Funct. Mater. 30 (2020) 2000473, https://doi.org/10.1002/adfm.202000473.
[9] T. Huang, G. Du, Y. Qi, J. Li, W. Zhong, Q. Yang, X. Zhang, M. Xu, A Prussian blue analogue as a long-life cathode for liquid-state and solid-state sodium-ion batteries, Inorg. Chem. Front. 7 (2020) 3938–3944, https://doi.org/10.1039/d0qi00872a.

[10] B. Xie, B. Sun, T. Gao, Y. Ma, G. Yin, P. Zuo, Recent progress of Prussian blue analogues as cathode materials for nonaqueous sodium-ion batteries, Coord. Chem. Rev. 460 (2022) 214478, https://doi.org/10.1016/j.ccr.2022.214478.
[11] Y. Li, A. Vasileiadis, Q. Zhou, Y. Lu, Q. Meng, Y. Li, P. Ombrini, J. Zhao, Z. Chen, Y. Niu, X. Qi, F. Xie, R. van der Jagt, S. Ganapathy, M.-M. Titirici, H. Li, L. Chen, M. Wagemaker, Y.-S. Hu, Origin of fast charging in hard carbon anodes, Nat. Energy 9 (2024) 134–142, https://doi.org/10.1038/s41560-023-01414-5.
[12] S. Zhang, N. Sun, X. Li, R.A. Soomro, B. Xu, Closed pore engineering of activated carbon enabled by waste mask for superior sodium storage, Energy Storage Mater. 66 (2024) 103183, https://doi.org/10.1016/j.ensm.2024.103183.
[13] Q. Lin, J. Qin, Y. Cao, X. Li, Y. Hong, M. Jin, J. Dong, W. Xiao, W. Li, J. Wang, X. Li, Optimization of $SbBi_x$ nanoparticles embedded in ultra-thin carbon networks for enhanced sodium/potassium storage, Chem. Eng. J. 474 (2023) 145717, https://doi.org/10.1016/j.cej.2023.145717.
[14] T. Zeng, X. Zhu, X. Wang, L. Zhang, Y. Ding, H. Jin, High capacity/reversible Fe/Sn alloys for Na-storage anodes enabled by thermal reaction and then anchoring on exfoliated graphite, J. Mater. Chem. A 11 (2023) 24712–24723, https://doi.org/10.1039/d3ta04905a.
[15] J.-E. Zhou, J. Chen, Y. Peng, Y. Zheng, A. Zeb, X. Lin, Metal-organic framework-derived transition metal sulfides and their composites for alkali-ion batteries: a review, Coord. Chem. Rev. 472 (2022) 214781, https://doi.org/10.1016/j.ccr.2022.214781.
[16] X. Zhang, M. Huang, Z. Peng, X. Sang, Y. Liu, X. Xu, Z. Xu, A. Zeb, Y. Wu, X. Lin, Metal-organic-framework derived Zn-V-based oxide with charge storage mechanism as high-performance anode material to enhance lithium and sodium storage, J. Colloid Interface Sci. 652 (2023) 1394–1404, https://doi.org/10.1016/j.jcis.2023.08.139.
[17] S. Eder, D.J. Yoo, W. Nogala, M. Pletzer, A. Santana Bonilla, A.J.P. White, K. E. Jelfs, M. Heeney, J.W. Choi, F. Glöcklhofer, Switching between local and global aromaticity in a conjugated macrocycle for high-performance organic sodium-ion battery anodes, Angew. Chem., Int. Ed. 59 (2020) 12958–12964, https://doi.org/10.1002/anie.202003386.
[18] C. Ma, L.-Y. Wang, M.-H. Shu, C.-C. Hou, K.-X. Wang, J.-S. Chen, Thiophene derivatives as electrode materials for high-performance sodium-ion batteries, J. Mater. Chem. A 9 (2021) 11530–11536, https://doi.org/10.1039/d1ta02181h.
[19] D. Chen, W. Zhang, K. Luo, Y. Song, Y. Zhong, Y. Liu, G. Wang, B. Zhong, Z. Wu, X. Guo, Hard carbon for sodium storage: mechanism and optimization strategies toward commercialization, Energy Environ. Sci. 14 (2021) 2244–2262, https://doi.org/10.1039/d0ee03916k.
[20] K. Li, J. Zhang, D. Lin, D.-W. Wang, B. Li, W. Lv, S. Sun, Y.-B. He, F. Kang, Q.-H. Yang, L. Zhou, T.-Y. Zhang, Evolution of the electrochemical interface in sodium ion batteries with ether electrolytes, Nat. Commun. 10 (2019) 725, https://doi.org/10.1038/s41467-019-08506-5.
[21] D.X. Luong, K.V. Bets, W.A. Algozeeb, M.G. Stanford, C. Kittrell, W. Chen, R. V. Salvatierra, M. Ren, E.A. McHugh, P.A. Advincula, Z. Wang, M. Bhatt, H. Guo, V. Mancevski, R. Shahsavari, B.I. Yakobson, J.M. Tour, Gram-scale bottom-up flash graphene synthesis, Nat. 577 (2020) 647–651, https://doi.org/10.1038/s41586-020-1938-0.
[22] L. Shi, Y. Sun, W. Liu, F. Zhao, G. Cheng, F. Zeng, J. Ding, Tailoring the microstructure and solid electrolyte interface of hard carbon to realize high-initial-coulombic-efficiency and high-rate sodium storage, Electrochim. Acta 459 (2023) 142557, https://doi.org/10.1016/j.electacta.2023.142557.
[23] C. Zheng, B. Jian, X. Xu, J. Zhong, H. Yang, S. Huang, Regulating microstructure of walnut shell-derived hard carbon for high rate and long cycling sodium-based dual-ion batteries, Chem. Eng. J. 455 (2023) 140434, https://doi.org/10.1016/j.cej.2022.140434.
[24] H. Chen, N. Sun, Q. Zhu, R.A. Soomro, B. Xu, Microcrystalline hybridization enhanced coal-based carbon anode for advanced sodium-ion batteries, Adv. Sci. 9 (2022) 2200023, https://doi.org/10.1002/advs.202200023.
[25] X. Chen, N. Sawut, K. Chen, H. Li, J. Zhang, Z. Wang, M. Yang, G. Tang, X. Ai, H. Yang, Y. Fang, Y. Cao, Filling carbon: a microstructure-engineered hard carbon for efficient alkali metal ion storage, Energy Environ. Sci. 16 (2023) 4041–4053, https://doi.org/10.1039/d3ee01154b.
[26] Z. Tang, R. Zhang, H. Wang, S. Zhou, Z. Pan, Y. Huang, D. Sun, Y. Tang, X. Ji, K. Amine, M. Shao, Revealing the closed pore formation of waste wood-derived hard carbon for advanced sodium-ion battery, Nat. Commun. 14 (2023) 6024, https://doi.org/10.1038/s41467-023-39637-5.
[27] F. Xie, Z. Xu, A.C.S. Jensen, H. Au, Y. Lu, V. Araullo-Peters, A.J. Drew, Y.S. Hu, M. M. Titirici, Hard-soft carbon composite anodes with synergistic sodium storage performance, Adv. Funct. Mater. 29 (2019) 1901072, https://doi.org/10.1002/adfm.201901072.
[28] Q. Meng, Y. Lu, F. Ding, Q. Zhang, L. Chen, Y.-S. Hu, Tuning the closed pore structure of hard carbons with the highest Na storage capacity, ACS Energy Lett. 4 (2019) 2608–2612, https://doi.org/10.1021/acsenergylett.9b01900.
[29] X. Lin, Y. Liu, H. Tan, B. Zhang, Advanced lignin-derived hard carbon for Na-ion batteries and a comparison with Li and K ion storage, Carbon 157 (2020) 316–323, https://doi.org/10.1016/j.carbon.2019.10.045.
[30] T. Xu, X. Qiu, X. Zhang, Y. Xia, Regulation of surface oxygen functional groups and pore structure of bamboo-derived hard carbon for enhanced sodium storage performance, Chem. Eng. J. 452 (2023) 139514, https://doi.org/10.1016/j.cej.2022.139514.
[31] H. Chen, N. Sun, Y. Wang, R.A. Soomro, B. Xu, One stone two birds: pitch assisted microcrystalline regulation and defect engineering in coal-based carbon anodes for sodium-ion batteries, Energy Storage Mater. 56 (2023) 532–541, https://doi.org/10.1016/j.ensm.2023.01.042.
[32] X. Yi, X. Li, J. Zhong, S. Wang, Z. Wang, H. Guo, J. Wang, G. Yan, Unraveling the mechanism of different kinetics performance between ether and carbonate ester electrolytes in hard carbon electrode, Adv. Funct. Mater. 32 (2022) 2209523, https://doi.org/10.1002/adfm.202209523.
[33] R. Dong, L. Zheng, Y. Bai, Q. Ni, Y. Li, F. Wu, H. Ren, C. Wu, Elucidating the mechanism of fast Na storage kinetics in ether electrolytes for hard carbon anodes, Adv. Mater. 33 (2021) 2008810, https://doi.org/10.1002/adma.202008810.
[34] H. Lu, X. Chen, Y. Jia, H. Chen, Y. Wang, X. Ai, H. Yang, Y. Cao, Engineering Al_2O_3 atomic layer deposition: Enhanced hard carbon-electrolyte interface towards practical sodium ion batteries, Nano Energy 64 (2019) 103903, https://doi.org/10.1016/j.nanoen.2019.103903.
[35] P. Bai, X. Han, Y. He, P. Xiong, Y. Zhao, J. Sun, Y. Xu, Solid electrolyte interphase manipulation towards highly stable hard carbon anodes for sodium ion batteries, Energy Storage Mater. 25 (2020) 324–333, https://doi.org/10.1016/j.ensm.2019.10.006.
[36] M.G. Stanford, K.V. Bets, D.X. Luong, P.A. Advincula, W. Chen, J.T. Li, Z. Wang, E. A. McHugh, W.A. Algozeeb, B.I. Yakobson, J.M. Tour, Flash graphene morphologies, ACS Nano 14 (2020) 13691–13699, https://doi.org/10.1021/acsnano.0c05900.
[37] Z. Zhao, J. Sun, Z. Li, X. Xu, Z. Zhang, C. Li, L. Wang, X. Meng, Rapid synthesis of efficient Mo-based electrocatalyst for the hydrogen evolution reaction in alkaline seawater with 11.28% solar-to-hydrogen efficiency, J. Mater. Chem. A 11 (2023) 10346–10359, https://doi.org/10.1039/d3ta01522j.
[38] P.M.F.J. Costa, U.K. Gautam, Y. Bando, D. Golberg, Direct imaging of Joule heating dynamics and temperature profiling inside a carbon nanotube interconnect, Nat. Commun. 2 (2011) 421, https://doi.org/10.1038/ncomms1429.
[39] J. Huang, S. Chen, Z. Ren, G. Chen, M. Dresselhaus, Real-time observation of tubule formation from amorphous carbon nanowires under high-bias Joule heating, Nano Lett. 6 (2006) 1699–1705, https://doi.org/10.1021/nl0609910.
[40] Y. Zhen, Y. Chen, F. Li, Z. Guo, Z. Hong, M.-M. Titirici, Ultrafast synthesis of hard carbon anodes for sodium-ion batteries, Proc. Natl. Acad. Sci. 118 (2021) e2111119118, doi: 10.1073/pnas.2111119118.
[41] X. Yin, Z. Lu, J. Wang, X. Feng, S. Roy, X. Liu, Y. Yang, Y. Zhao, J. Zhang, Enabling fast Na^+ transfer kinetics in the whole-voltage-region of hard-carbon anodes for ultrahigh-rate sodium storage, Adv. Mater. 34 (2022) 2109282, https://doi.org/10.1002/adma.202109282.
[42] J. Zhao, X.X. He, W.H. Lai, Z. Yang, X.H. Liu, L. Li, Y. Qiao, Y. Xiao, L. Li, X. Wu, S. L. Chou, Catalytic defect-repairing using manganese ions for hard carbon anode with high-capacity and high-initial-coulombic-efficiency in sodium-ion batteries, Adv. Energy Mater. 13 (2023) 2300444, https://doi.org/10.1002/aenm.202300444.
[43] Y. Wang, N. Xiao, Z. Wang, H. Li, M. Yu, Y. Tang, M. Hao, C. Liu, Y. Zhou, J. Qiu, Rational design of high-performance sodium-ion battery anode by molecular engineering of coal tar pitch, Chem. Eng. J. 342 (2018) 52–60, https://doi.org/10.1016/j.cej.2018.01.098.
[44] M. Liu, F. Wu, Y. Gong, Y. Li, Y. Li, X. Feng, Q. Li, C. Wu, Y. Bai, Interfacial-catalysis-enabled layered and inorganic-rich SEI on hard carbon anodes in ester electrolytes for sodium-ion batteries, Adv. Mater. 35 (2023) 2300002, https://doi.org/10.1002/adma.202300002.
[45] Y. Chen, H. Sun, X.X. He, Q. Chen, J.H. Zhao, Y. Wei, X. Wu, Z. Zhang, Y. Jiang, S. L. Chou, Pre-oxidation strategy transforming waste foam to hard carbon anodes for boosting sodium storage performance, Small (2023) 2307132, https://doi.org/10.1002/smll.202307132.
[46] Q. Wang, X. Zhu, Y. Liu, Y. Fang, X. Zhou, J. Bao, Rice husk-derived hard carbons as high-performance anode materials for sodium-ion batteries, Carbon 127 (2018) 658–666, https://doi.org/10.1016/j.carbon.2017.11.054.
[47] Q. He, H. Chen, X. Chen, J. Zheng, L. Que, F. Yu, J. Zhao, Y. Xie, M. Huang, C. Lu, J. Meng, X. Zhang, Tea-derived sustainable materials, Adv. Funct. Mater. 34 (2024) 2470062, https://doi.org/10.1002/adfm.202310226.
[48] Y. Chen, F. Li, Z. Guo, Z. Song, Y. Lin, W. Lin, L. Zheng, Z. Huang, Z. Hong, M.-M. Titirici, Sustainable and scalable fabrication of high-performance hard carbon anode for Na-ion battery, Journal of Power Sources 557 (2023) 232534, https://doi.org/10.1016/j.jpowsour.2022.232534.
[49] Z. Lu, J. Wang, W. Feng, X. Yin, X. Feng, S. Zhao, C. Li, R. Wang, Q.A. Huang, Y. Zhao, Zinc single-atom-regulated hard carbons for high-rate and low-temperature sodium-ion batteries, Adv. Mater. 35 (2023) 2211461, https://doi.org/10.1002/adma.202211461.
[50] D. Cheng, Z. Li, M. Zhang, Z. Duan, J. Wang, C. Wang, Engineering ultrathin carbon layer on porous hard carbon boosts sodium storage with high initial Coulombic efficiency, ACS Nano 17 (2023) 19063–19075, https://doi.org/10.1021/acsnano.3c04984.
[51] J. Yan, H. Li, K. Wang, Q. Jin, C. Lai, R. Wang, S. Cao, J. Han, Z. Zhang, J. Su, K. Jiang, Ultrahigh phosphorus doping of carbon for high-rate sodium ion batteries anode, Adv. Energy Mater. 11 (2021) 2003911, https://doi.org/10.1002/aenm.202003911.
[52] Y. Zhao, Z. Hu, C. Fan, P. Gao, R. Zhang, Z. Liu, J. Liu, J. Liu, Novel structural design and adsorption/insertion coordinating quasi-metallic Na storage mechanism toward high-performance hard carbon anode derived from carboxymethyl cellulose, Small 19 (2023) 2303296, https://doi.org/10.1002/smll.202303296.
[53] M. Guo, H. Zhang, Z. Huang, W. Li, D. Zhang, C. Gao, F. Gao, P. He, J. Wang, W. Chen, X. Chen, M. Terrones, Y. Wang, Liquid template assisted activation for "egg puff"-like hard carbon toward high sodium storage performance, Small 19 (2023) 2302583, https://doi.org/10.1002/smll.202302583.
[54] S. Li, H. Yuan, C. Ye, Y. Wang, L. Wang, K. Ni, Y. Zhu, Sucrose-derived hard carbon wrapped with reduced graphene oxide as a high-performance anode for sodium-ion

batteries, J. Mater. Chem. A 11 (2023) 9816–9823, https://doi.org/10.1039/d3ta00898c.
[55] H. Fang, S. Gao, M. Ren, Y. Huang, F. Cheng, J. Chen, F. Li, Dual-function presodiation with sodium diphenyl ketone towards ultra-stable hard carbon anodes for sodium-ion batteries, Angew. Chem., Int. Ed. 62 (2022) e202214717, doi: 10.1002/anie.202214717.
[56] M. Song, Q. Song, T. Zhang, X. Huo, Z. Lin, Z. Hu, L. Dong, T. Jin, C. Shen, K. Xie, Growing curly graphene layer boosts hard carbon with superior sodium-ion storage, Nano Res. 16 (2023) 9299–9309, https://doi.org/10.1007/s12274-023-5539-8.
[57] Z. Lu, C. Geng, H. Yang, P. He, S. Wu, Q.-H. Yang, H. Zhou, Step-by-step desolvation enables high-rate and ultra-stable sodium storage in hard carbon anodes, Proc. Natl. Acad. Sci. 119 (2022) e2210203119, doi: 10.1073/pnas.
[58] X. Feng, Y. Li, Y. Li, M. Liu, L. Zheng, Y. Gong, R. Zhang, F. Wu, C. Wu, Y. Bai, Unlocking the local structure of hard carbon to grasp sodium-ion diffusion behavior for advanced sodium-ion battery, Energy Environ. Sci. 17 (2024) 1387–1396, https://doi.org/10.1039/D3EE03347C.
[59] Z. Song, F. Li, L. Mao, W. Lin, L. Zheng, Y. Huang, M. Wei, Z. Hong, Sustainable fabrication of a practical hard carbon anode for a sodium-ion battery with unprecedented long cycle life, ACS Sustainable Chem. Eng. 11 (2023) 15020–15030, https://doi.org/10.1021/acssuschemeng.3c03765.
[60] L. Yan, G. Zhang, J. Wang, Q. Ren, L. Fan, B. Liu, Y. Wang, W. Lei, D. Ruan, Q. Zhang, Z. Shi, Revisiting electrolyte kinetics differences in sodium ion battery: Are esters really inferior to ethers? Energy Environ. Mater. 6 (2022) e12523.
[61] M.K. Sadan, H. Kim, C. Kim, S.H. Cha, K.-K. Cho, K.-W. Kim, J.-H. Ahn, H.-J. Ahn, Enhanced rate and cyclability of a porous Na3V2(PO4)3 cathode using dimethyl ether as the electrolyte for application in sodium-ion batteries, J. Mater. Chem. A 8 (2020) 9843–9849, https://doi.org/10.1039/d0ta02721a.
[62] Y. Wang, P. Bai, B. Li, C. Zhao, Z. Chen, M. Li, H. Su, J. Yang, Y. Xu, Ultralong cycle life organic cathode enabled by ether-based electrolytes for sodium-ion batteries, Adv. Energy Mater. 11 (2021) 2101972, https://doi.org/10.1002/aenm.202101972.
[63] Z. Li, Z. Jian, X. Wang, I.A. Rodríguez-Pérez, C. Bommier, X. Ji, Hard carbon anodes of sodium-ion batteries: undervalued rate capability, Chem. Commun. 53 (2017) 2610–2613, https://doi.org/10.1039/c7cc00301c.
[64] Y. Huang, X. Zhong, X. Hu, Y. Li, K. Wang, H. Tu, W. Deng, G. Zou, H. Hou, X. Ji, Rationally designing closed pore structure by carbon dots to evoke sodium storage sites of hard carbon in low-potential region, Adv. Funct. Mater. 2308392 (2023), https://doi.org/10.1002/adfm.202308392.
[65] J.L. Xia, D. Yan, L.P. Guo, X.L. Dong, W.C. Li, A.H. Lu, Hard carbon nanosheets with uniform ultramicropores and accessible functional groups showing high realistic capacity and superior rate performance for sodium-ion storage, Adv. Mater. 32 (2020) 2000447, https://doi.org/10.1002/adma.202000447.
[66] J. Yang, X. Wang, W. Dai, X. Lian, X. Cui, W. Zhang, K. Zhang, M. Lin, R. Zou, K. P. Loh, Q.-H. Yang, W. Chen, From micropores to ultra-micropores inside hard carbon: toward enhanced capacity in room-/low-temperature sodium-ion storage, Nano-Micro Lett. 13 (2021) 98, https://doi.org/10.1007/s40820-020-00587-y.
[67] G. Li, J. Wang, J. Chu, M. Li, Z. Hu, F. Wang, Y. Han, T. Cai, Z. Song, Ultrafast and ultrastable Na-ion storage in zero-strain sodium perylenetetracarboxylate anode enabled by ether electrolyte, Energy Storage Mater. 47 (2022) 1–12, https://doi.org/10.1016/j.ensm.2022.01.053.
[68] Z. Wang, H. Yang, Y. Liu, Y. Bai, G. Chen, Y. Li, X. Wang, H. Xu, C. Wu, J. Lu, Analysis of the stable interphase responsible for the excellent electrochemical performance of graphite electrodes in sodium-ion batteries, Small 16 (2020) 2003268, https://doi.org/10.1002/smll.202003268.
[69] G.G. Eshetu, T. Diemant, M. Hekmatfar, S. Grugeon, R.J. Behm, S. Laruelle, M. Armand, S. Passerini, Impact of the electrolyte salt anion on the solid electrolyte interphase formation in sodium ion batteries, Nano Energy 55 (2019) 327–340, https://doi.org/10.1016/j.nanoen.2018.10.040.
[70] M. Ma, H. Cai, C. Xu, R. Huang, S. Wang, H. Pan, Y.S. Hu, Engineering solid electrolyte interface at nano-scale for high-performance hard carbon in sodium-ion batteries, Adv. Funct. Mater. 31 (2021) 2100278, https://doi.org/10.1002/adfm.202100278.
[71] W. Li, X. Guo, K. Song, J. Chen, J. Zhang, G. Tang, C. Liu, W. Chen, C. Shen, Binder-induced ultrathin SEI for defect-passivated hard carbon enables highly reversible sodium-ion storage, Adv. Energy Mater. 13 (2023) 2300648, https://doi.org/10.1002/aenm.202300648.
[72] S. Choudhury, S. Wei, Y. Ozhabes, D. Gunceler, M.J. Zachman, Z. Tu, J.H. Shin, P. Nath, A. Agrawal, L.F. Kourkoutis, T.A. Arias, L.A. Archer, Designing solid-liquid interphases for sodium batteries, Nat. Commun. 8 (2017) 898, https://doi.org/10.1038/s41467-017-00742-x.